JACS
JOURNAL OF THE AMERICAN CHEMICAL SOCIETY
Article
pubs.acs.org/JACS

Facet-Dependent Photoelectrochemical Performance of TiO_2 Nanostructures: An Experimental and Computational Study

Chuanhao Li,[†,§] Christopher Koenigsmann,[‡,§] Wendu Ding,[‡] Benjamin Rudshteyn,[‡] Ke R. Yang,[‡] Kevin P. Regan,[‡] Steven J. Konezny,[‡] Victor S. Batista,[‡] Gary W. Brudvig,[‡] Charles A. Schmuttenmaer,*[,‡] and Jae-Hong Kim*[,†]

[†]Department of Chemical and Environmental Engineering, Yale University, New Haven, Connecticut 06520-8276, United States
[‡]Yale Energy Sciences Institute and Department of Chemistry, Yale University, New Haven, Connecticut 06520-8107, United States

Supporting Information

ABSTRACT: The behavior of crystalline nanoparticles depends strongly on which facets are exposed. Some facets are more active than others, but it is difficult to selectively isolate particular facets. This study provides fundamental insights into photocatalytic and photoelectrochemical performance of three types of TiO_2 nanoparticles with predominantly exposed {101}, {010}, or {001} facets, where 86−99% of the surface area is the desired facet. Photodegradation of methyl orange reveals that {001}-TiO_2 has 1.79 and 3.22 times higher photocatalytic activity than {010} and {101}-TiO_2, respectively. This suggests that the photochemical performance is highly correlated with the surface energy and the number of under-coordinated surface atoms. In contrast, the photoelectrochemical performance of the faceted TiO_2 nanoparticles sensitized with the commercially available MK-2 dye was highest with {010}-TiO_2 which yielded an overall cell efficiency of 6.1%, compared to 3.2% for {101}-TiO_2 and 2.6% for {001}-TiO_2 prepared under analogous conditions. Measurement of desorption kinetics and accompanying computational modeling suggests a stronger covalent interaction of the dye with the {010} and {101} facets compared with the {001} facet. Time-resolved THz spectroscopy and transient absorption spectroscopy measure faster electron injection dynamics when MK-2 is bound to {010} compared to other facets, consistent with extensive computational simulations which indicate that the {010} facet provides the most efficient and direct pathway for interfacial electron transfer. Our experimental and computational results establish for the first time that photoelectrochemical performance is dependent upon the binding energy of the dye as well as the crystalline structure of the facet, as opposed to surface energy alone.

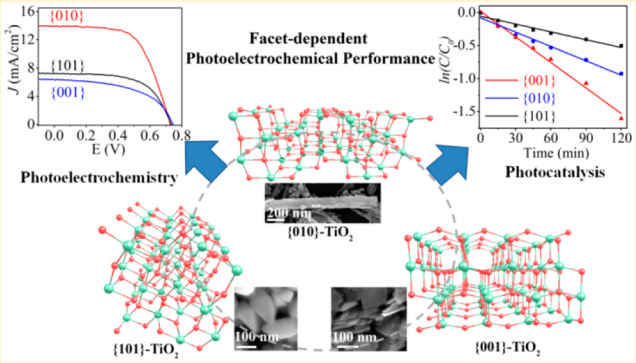

1. INTRODUCTION

Solar energy is a promising pathway toward addressing the global challenges of alternative energy needs and environmental sustainability.[1] Semiconductor-based materials have been instrumental in converting solar irradiation to energy by facilitating the absorption of photons and the subsequent generation of photoelectrons and holes.[2] These can be harnessed to either generate electricity,[3] initiate photodriven reactions, produce chemical fuels (e.g., hydrogen or methanol),[4] or form free radical species.[5] Among many promising semiconductor materials, nanoscale titanium dioxide (TiO_2) has been broadly employed in photocatalysis and photoelectrochemical cells due to its advantageous electronic properties, relatively high electron mobility, photochemical stability, and abundance.[6]

The photocatalytic performance of TiO_2 nanoparticles (NPs) depends largely upon the physicochemical properties of the material including the surface area-to-volume ratio, particle size, morphology, crystallinity, and surface structure.[7,8] Catalytic reactions occur at the surface of NPs, and thus, catalytic activity is largely dependent upon crystalline structure and exposed facets.[9−11] In the case of TiO_2, the anatase phase has received the most attention because of its relatively high catalytic activity and electron mobility compared to the rutile and brookite phases.[12] In terms of surface structure, computational and experimental results indicate that the {101}, {010}, and {001} surface facets of anatase TiO_2 exhibit increasing average surface energies of 0.44, 0.53, and 0.90 J/m^2, respectively.[13,14] Studies of the facet-dependent reactivity on single-crystals and NPs have demonstrated that photocatalytic performance is measurably increased on the higher energy {001} and {010} facets.[13−16] This has been attributed to the high surface energy and the predominance of surface Ti^{4+} sites with five-fold coordination spheres, which are expected to strongly interact with adsorbates on the surface during catalytic reactions.[8,16]

Several researchers have explored routes to synthesize anatase TiO_2 via hydrothermal methods with reliable and predictable

Received: October 29, 2014
Published: January 6, 2015

 © 2015 American Chemical Society
DOI: 10.1021/ja5111078
J. Am. Chem. Soc. 2015, 137, 1520−1529

control over the relative exposure of the {001}, {010}, and {101} facets.[13,14,17−22] For example, the growth of NPs with the highest energy {001} facets exposed has been achieved by adding F^- ions in the growth media to cap the {001} facet thereby leading to selective growth along the {101} and {010} facets. Facet purity of over 80% has been achieved with nanosheets and nanodisks as predominant morphologies by combining F^- with organic capping agents.[15,23] It has been reported in all of these cases that increasing the fraction of {001} facets enhances photocatalytic activity.

Although the facet-dependent performance of TiO_2 has been well studied in the realm of photocatalytic reactions, there are few reports regarding the facet-dependent photoelectrochemical performance particularly in the case of dye-sensitized systems. In these systems, wide-band gap semiconductors such as TiO_2 are sensitized by covalently attached organic or inorganic chromophores, which absorb light in the visible spectrum.[2,24−26] Photoexcitation of the chromophore results in an ultrafast interfacial electron transfer (IET) into the conduction band of the semiconductor leading to charge separation.[27] The resulting hole localized on the chromophore can either be utilized for catalytic reactions such as water splitting[28] or transferred via an electrolyte system to produce electrical current in the case of dye-sensitized solar cells (DSSCs).[29] The charge-separation efficiency and photoelectrochemical performance are, therefore, largely dependent on the relative rates of electron injection and recombination, which are affected not only by the properties of the semiconductor itself but also its interaction with the chromophore.[27,29,30] Specifically, the IET dynamics depend strongly upon the interplay among the driving force for electron injection,[31] the strength of the covalent interaction,[32,33] the nature of the chromophore's anchoring group,[34,35] anchoring geometry,[36,37] and the surface density of chromophores[38] as well as the surface structure, morphology, and crystallinity of the TiO_2.[39,40] Therefore, studying the facet-dependent photoelectrochemical performance in a rational manner is challenging since all of these factors must be considered.

A recent and promising approach has been to study photoelectrochemical performance using DSSC devices because they are well-characterized, inexpensive, and easy to assemble.[41−43] Given the high photocatalytic activity of the {001} facet, prior studies have focused on examining the facet-dependent DSSC performance of TiO_2 NPs with different percentages of the {001} facet exposed relative to the {101} facet.[43−45] For example, a recent report found that increasing the exposure of the {001} facet from 10% in one shape of NP to 80% in another resulted in small but measurable increase of ∼8% in DSSC efficiency.[44] In another report, TiO_2 nanosheets with 75% exposure of the {001} facet showed an enhanced efficiency of 4.6% relative to 4.2% measured for {101} terminated NPs.[43] In both cases, accurate interpretation of the facet-dependency was difficult since the NPs in these studies consisted of mixtures of the {101} and {001} facets with the desired facet representing 80% or less of the total surface area. Also, variations in performance were not significantly larger than typical device-to-device variations for DSSCs reported in the literature.[2] From a computational perspective, a recent study comparing the calculated recombination rates of Ru-based C101 dye (Dyesol Ltd.) bound to the {101} and {001} surfaces suggested that the adsorption of the dye on the {001} facet may slow recombination when compared to the adsorption on the {101} facet leading to higher efficiencies.[42] However, neither spectroscopic measurements of the relative electron injection and recombination rates nor simulations of electron injection dynamics have yet been performed as a function of surface facet.

In this report, we performed a comprehensive study of the facet-dependent performance including (i) photocatalysis measurements, (ii) characterization of photoelectrochemical performance in DSSC devices, (iii) time-resolved spectroscopy, and (iv) first-principles calculations of {101}, {001}, and {010} terminated NPs with >86% exposure of the desired facet. To the best of our knowledge, this is the first systematic study of the facet-dependent performance highlighting contrasting trends in photochemical and photoelectrochemical performance in anatase TiO_2 nanoparticles. The UV-photodegradation of methyl orange established that the {001} terminated NPs achieved the highest photocatalytic performance of the three facets. Interestingly, the photoelectrochemical performance of the faceted TiO_2 NPs sensitized with the MK-2 dye in DSSC devices varied in a different manner: The devices utilizing the {010} terminated NPs exhibited the highest photoelectrochemical performance of 6.1%, which was 2-fold higher than that of the {101} and {001} NPs (3.2% and 2.6%, respectively). This is in stark contrast with the photocatalytic results and with prior photoelectrochemical results.[43−45] Time-resolved THz and transient absorption (TA) spectroscopies measured more efficient electron injection and faster recombination dynamics with {010}-faceted TiO_2. Computational results further confirmed that the photoelectrochemical performance and injection efficiency can be attributed to the structure of the different facets, which promotes unique pathways for IET.

2. EXPERIMENTAL METHODS

2.1. Synthesis and Characterization. The synthesis of the {101}, {010}, and {001}-TiO_2 nanoparticles was accomplished by hydrothermal methods. Characterization of the materials including their size and morphology, specific surface area, and band gap was accomplished by scanning electron microscopy (SEM), transmission electron microscopy (TEM), nitrogen adsorption isotherms, and UV−vis spectroscopy. The details of the synthesis and characterization, time-resolved spectroscopy, and computational methods can be found in Sections 1−3 of the Supporting Information, respectively.

2.2. Photodegradation Experiments. Methyl orange (MO) was used as a model compound for organic environmental contaminants to test the facet-dependent photocatalytic activity. In a typical measurement, TiO_2 powder (∼4 mg) was suspended in 20 mL of a 10 ppm aqueous MO solution prepared with ultrapure water (18.2 MΩ·cm). Five 4-W "black lights" were used as the UV light source. The light intensity was 4.9 $mW \cdot cm^{-2}$ as measured with a photometer (PMA2200, Solar light Co.) equipped with the UV-A detector (PMA2110). Prior to irradiation, the suspension was stirred in the dark for 4 h to establish an adsorption/desorption equilibrium, after which the photocatalytic degradation of MO was initiated. Photodegradation was monitored by measuring the absorbance of the solution at 477 nm. Commercially available anatase TiO_2 nanoparticles with a particle size of <25 nm (Sigma-Aldrich, 99.7%, 45−55 $m^2 \cdot g^{-1}$) were employed as a common standard for photocatalytic performance.

2.3. Photoelectrochemical Performance. Construction of MK-2 sensitized DSSCs was based on previously reported methods.[34] In brief, the as-prepared TiO_2 nanoparticles were rendered into pastes by grinding the dry powders in the presence of glacial acetic acid (JT Baker, ACS reagent), α-terpineol (Alfa Aesar, 96%) and ethanol utilizing the method described by Grätzel and co-workers.[46] Photoanodes were prepared by first pretreating the surface of TEC 15 FTO coated glass (Hartford Glass) with $TiCl_4$ and subsequently depositing thin films utilizing the doctor-blading technique. After annealing at 450 °C, the films maintained an approximate thickness of 7 μm as measured by profilometry. Films were sensitized with the MK-2 dye (Sigma-Aldrich, 95%) by immersing the films into a

DOI: 10.1021/ja5111078
J. Am. Chem. Soc. 2015, 137, 1520−1529

solution consisting of 0.3 mM MK-2 dye in anhydrous toluene for a period of 16 h. The electrolyte was prepared from a combination of 1,2-dimethyl-3-propylimidazolium iodide (DMPII, TCI, 98%, 0.6 M), lithium iodide (anhydrous, 99.95%, Alfa Aesar, 0.1 M), iodine (pure, Acros Organics, 0.2 M), 4-*tert*-butylpyridine (TBP, Sigma-Aldrich, 96%, 0.5 M), and anhydrous acetonitrile as the solvent (Omni Solv, EMD Millipore). DSSC performance was characterized by current density−voltage (J−V) curves and external quantum efficiency (EQE) spectra measured using a Keithley 2400-C source-meter and a solar simulator (Newport) equipped with a 1000 W ozone-free xenon lamp and AM1.5G filter. The light intensity was adjusted with a diode calibrated by Newport to ASTM E948-09 and E1021-06 standards. Conductivities of faceted TiO_2 films prepared analogously to those employed in DSSC devices prepared on sapphire substrates with thermally evaporated gold contacts were obtained on an Agilent B1500A semiconductor device analyzer with medium-power source-measurement units paired with atto-sense and switch units for high-resolution current sensing.

2.4. Dye Loading and Desorption Experiments. Dye loading experiments were performed on as-prepared TiO_2 nanoparticle powders, which were preheated to 120 °C to remove excess moisture. The powders were dispersed by sonication into either 0.3 mM MK-2 in anhydrous toluene or 0.3 mM benzoic acid in anhydrous ethanol, and the resulting suspensions were stirred at 1100 rpm for a period of 16 h. The loaded powder was then removed by centrifugation. The dye loading was quantified by measuring the changes in the concentration of the loading solution before and after adsorption utilizing UV−vis spectrophotometry. The desorption studies were performed with MK-2 sensitized TiO_2 films utilizing a method that is described in detail in ref 34. The films were prepared identically to those employed in the DSSC devices, however the thickness was reduced from 7 to 3 μm to avoid effects of diffusion of the dye through the films. Subsequently, desorption experiments were performed by immersing the sensitized films into a solution containing 0.5 vol % water dissolved in anhydrous dimethylformamide (DMF, Sigma-Aldrich, <0.005% H_2O, 99.8%).[34] The time-dependent desorption of the dye was measured *in situ* by UV−vis spectrophotometry over a period of 90 min to determine the quantity of dye desorbed into the H_2O-DMF solution.

3. RESULTS AND DISCUSSION

3.1. Materials Characterization. Representative SEM images of faceted TiO_2 samples are shown in Figure 1 highlighting the octahedral (i.e., nanoctahedra), belt-like (i.e., nanobelts), and plate-like (i.e., nanoplates) morphologies of the {101}, {010}, and {001} NPs, respectively. We also performed high-resolution transmission electron microscopy (HRTEM) in order to assign the surfaces of the nanoparticles with corresponding crystalline facets. The results are summarized in Figure S2. The exposure of the predominant facet was calculated based upon the morphology and dimensions of the as-prepared NPs (cf. Supporting Information, Section 5), and the results are presented in Table 1. In all cases, the desired facet represents >86% of the total surface area of the NPs and is nearly 100% in the case of the {101} facet. Powder X-ray diffraction (XRD, cf. Figure S3) measurements confirmed the quality and purity of the samples and indicated that each nanoparticle sample consisted of pure anatase TiO_2.

Given the variations in particle size and dimension, the specific surface area (SSA) of the faceted NP samples was experimentally measured by nitrogen adsorption and desorption isotherms. The results (Table 1) show that the SSA of the nanoplates is roughly 20% and 13% higher than the nanoctahedra and nanobelts, respectively. This increase is readily attributed to the thickness of the NPs, which was determined to be approximately 6, 17, 75 nm for the nanoplates, nanobelts, and nanoctahedra, respectively. The bandgaps of these NPs, determined

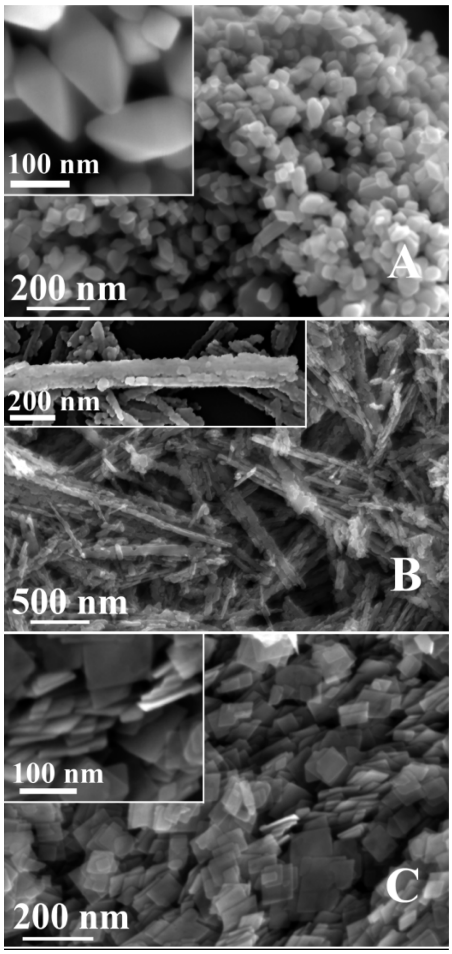

Figure 1. SEM images of (A) {101}-TiO_2, (B) {010}-TiO_2, and (C) {001}-TiO_2.

Table 1. Physicochemical Properties of the Prepared Faceted TiO_2

sample	morphology	specific surface area ($m^2 \cdot g^{-1}$)	approximate % of predominant facet[a]	bandgap (eV)
{101}	nanoctahedra	54	99	3.29
{010}	nanobelts	61	91	3.28
{001}	nanoplate	70	86	3.28

[a]The calculation method is described in Section 5 of the Supporting Information.

from diffuse reflectance spectroscopy (Figure S4),[16] were found to be essentially identical with a value of approximately 3.28 eV consistent with prior results.[47] The similarity in the bandgaps of the {101}, {010}, and {001} nanoparticles and the high percentage of the desired facet in each case is advantageous for the purpose of this study since the influence of the surface facet is a predominant factor in determining photocatalytic and photoelectrochemical performance. This is especially relevant since previous reports employ materials with either lower relative percentages of the desired facet exposed (<80%)[43,44] or were performed with commercial NPs (e.g., Degussa P25), which are a mixture of the anatase and rutile phases and have disordered surfaces.[45]

3.2. Photochemical Activity. Figures S5A−C show the UV−vis absorption spectra of methyl orange as a function of irradiation time for the three TiO_2 samples, and Figure S5E shows the change in the relative concentration of methyl orange as a function of time. It is evident that the rate of

DOI: 10.1021/ja5111078
J. Am. Chem. Soc. 2015, 137, 1520−1529

photodegradation increases in the following order: {101} < {010} < {001}. The photocatalytic rate constants of methyl orange degradation were calculated from fits of $\ln(C/C_0)$ with respect to time shown in Figure 2. The pseudo-first-order rate

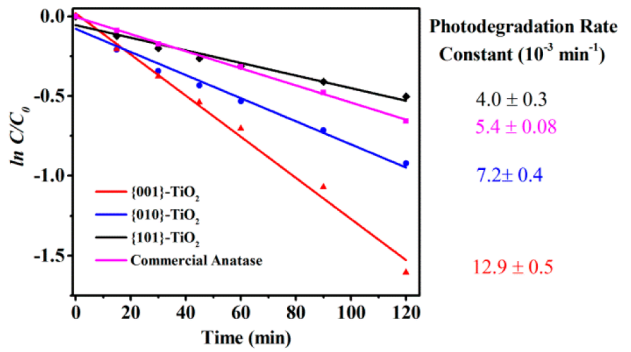

Figure 2. Pseudo-first-order plots of the photodegradation of methyl orange using different faceted TiO_2 and associated photodegradation rate constants.

constants reported in Figure 2 reveal that the {001}-TiO_2 provides 1.79 and 3.22 times higher degradation rate than {010}- and {101}-TiO_2, respectively. Given the differences in SSA, the rate constants were normalized with respect to the geometric surface area of the catalysts utilized during each reaction. The normalized results summarized in Table S1 still show the same trend in performance and confirm that the {001}-TiO_2 has the most efficient photodegradation activity. In addition, the catalytic activities and trend in performance measured herein are consistent with those measured in prior reports highlighting the quality of the TiO_2 nanostructures.[48,49] In this case and in prior reports, the photocatalytic performance depends largely upon the surface energy and the relative number of Ti^{4+} sites with five-fold coordination environments, both of which are greater on the {001} and {010} facets relative to the {101} facet.[8,16] We note that the commercial anatase TiO_2 nanoparticles and the as-prepared {101} nanoctahedra provide comparable photocatalytic performance after normalizing to surface area. This is expected since the commercial NPs adopt bipyramidal morphologies, which predominantly exposes the lowest energy {101} facet in a fashion analogous to our nanoctahedra.[6]

3.3. Photoelectrochemical Performance. We employed the MK-2 dye (see Scheme S4 in the Supporting Information for its structure) as a prototypical, state-of-the-art, and commercially available organic dye to sensitize TiO_2 NPs. Recently, there has been a growing interest in organic dyes because they avoid the need for noble metals, have high extinction coefficients, are easier to synthesize, and are less susceptible to desorption from the surface of TiO_2 in the presence of water than commonly used Ru-based dyes.[50]

The photoelectrochemical activity of DSSC devices assembled with MK-2 dye and the three different types of TiO_2 NPs were measured to evaluate the facet-dependent performance. The photovoltaic parameters and corresponding standard deviation determined from the performance of six separate devices for each NP sample are summarized in Table 2. Figure 3 displays $J-V$ curves and EQE spectra of representative devices.

The photoelectrochemical performance of the DSSC devices revealed a significant dependence on the surface facets of the NPs. Interestingly, the {010}-TiO_2 cells showed the highest cell efficiency. It was 6.1%, which is 2-fold larger than the {101}-TiO_2 and {001}-TiO_2 devices (3.2% and 2.6%, respectively).

Table 2. Photovoltaic Performance of DSSCs Prepared with Three Faceted TiO_2 Sensitized With MK-2 under Simulated One-Sun Illumination (AM1.5G)

sample	conductivity of films (Ω^{-1} cm^{-1})	η^a (%)	$V_{oc}{}^a$ (V)	$J_{sc}{}^a$ (mA cm^{-2})	FF^a (%)	max. EQE^b (%)
{101}	4.8×10^{-8}	3.2	0.736	7.1	60	28.4
{010}	1.1×10^{-7}	6.1	0.729	13.6	61	41.9
{001}	2.7×10^{-6}	2.6	0.737	6.5	54	30.3

[a]Photovoltaic parameters as the average of measurements collected from six separate DSSC devices prepared from each nanoparticle sample. [b]The EQE values are reported at 476 nm.

The increased efficiency strongly correlates with the short circuit current density (J_{sc}), which is 2-fold higher in the case of the {010}-TiO_2 relative to the {001} and {101} samples. The open circuit voltage (V_{oc}) values were essentially identical with a value of 734 ± 5 mV determined from the average V_{oc} from the three sets of devices. This is not surprising since the V_{oc} is determined largely by the potential difference of the TiO_2 quasi-Fermi level and the redox potential of the electrolyte. It is reasonable to expect that their conduction band edges would also be identical, since the band gaps of the TiO_2 materials were shown to be identical and all of the nanoparticles were pretreated with glacial acetic acid (see Section 2.3) to protonate the surfaces. In addition, the {001}, {010}, and {101} NPs have comparable fill factors (FFs) of about 55−60%, which was consistent with the negligible differences observed in the series and shunt resistances determined from fits of the $J-V$ curves. In addition, we also determined that the J_{sc} and FF were not correlated with the measured conductivity of the films (Table 2), indicating that the photoelectrochemical performance was primarily determined by the surface structure of the NPs rather than any influence of the morphology on the film conductivity.

To investigate the correlation between device efficiency and the measured J_{sc} values, we collected EQE spectra from three representative devices, which are shown in Figure 3B. The results clearly demonstrate that the {010}-TiO_2 maintains a higher EQE relative to the other facets over the spectral range that is associated with the MK-2 dye's absorption spectrum (Figure S6).[34] At the peak of the EQE spectra (476 nm), the EQE of the {010}-TiO_2 was determined to be 41.9%, which was significantly higher than the values of 28.4% and 30.3% for the {101}- and {001}-TiO_2, respectively (Table 2).

To confirm that the trend in photoelectrochemical performance was not associated with the dye loading, UV−vis spectroscopy was performed on 3.5 and 7.0 μm thick films of the faceted NPs, and the results confirmed that the absorbance of the films was >3 between 350 and 575 nm, regardless of the thickness. This suggests that more than 99.9% of the photons at the peak absorption of the dye were absorbed within the first 3.5 μm regardless of the dye loading and surface area. The geometric surface area of the films was estimated by measuring the loading of benzoic acid onto 7 μm thick films of the faceted NPs. The loading of benzoic acid was determined to be 30, 57, and 94 nmol·cm^{-2} for the {101}-, {010}-, and {001}-TiO_2 NPs, respectively. As expected, there was no significant correlation between the trend in photoelectrochemical performance and the trend in loading, indicating that the performance is dependent on the surface structure and not on factors such as the geometric surface area or dye loading of the film.

It is also important to consider the presence of small fractions of other surface facets present on the as-prepared TiO_2 NPs.

DOI: 10.1021/ja5111078
J. Am. Chem. Soc. 2015, 137, 1520−1529

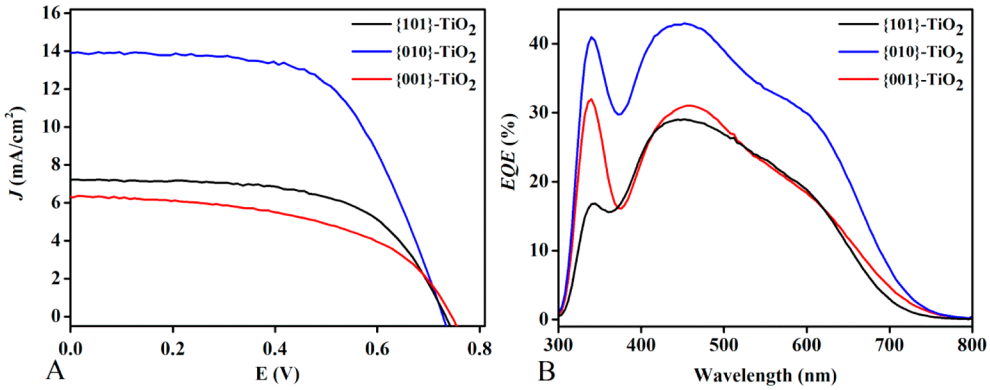

Figure 3. Current density vs voltage (J−V) under simulated one-sun illumination (A) (AM1.5G) and (B) EQE spectra for DSSC devices prepared with {101}-TiO_2, {010}-TiO_2, and {001}-TiO_2.

Table 3. Dye Adsorption Parameters for Different TiO_2 Facets

surface	surface Ti^{4+} density[a] (sites·nm^{-2})	MK-2 surface coverage (molecules·nm^{-2})	benzoic acid surface coverage (molecules·nm^{-2})	k_{des} (s^{-1})	calculated adsorption energy[b] (kcal/mol) monodentate	calculated adsorption energy[b] (kcal/mol) bidentate
{101}	5.5	0.84	0.53	9.7×10^{-4}	−4	21
{010}	5.6	0.87	0.65	8.2×10^{-4}	−10	5
{001}	7.0	0.51	0.29	3.0×10^{-2}	20	33

[a]The surface Ti^{4+} density was calculated for the number of five-fold coordination sites on computationally relaxed surfaces as described in the Supporting Information. [b]The adsorption energy is calculated for the adsorption of a single benzoic acid molecule via the most stable monodentate or bridging bidentate binding geometries on the respective hydrated TiO_2 surface.

For the cases of {010}- and {101}-TiO_2, the electron microscopy and XRD results indicate that the surface coverage of the desired facet is >91%, and thus, the presence of other facets is expected to have minimal effects on photoelectrochemical performance. On the other hand, in the case of the {001}-TiO_2 nanoparticles, the corresponding presence of 14% of {101} facets may have a small effect on the photoelectrochemical performance. However, prior reports have shown that nanoparticles with {101} and {001} surfaces exhibit similar photoelectrochemical performance.[43,44] For example, it was shown that nanoparticles prepared with surface coverages of the {001} facet ranging from 14−80% displayed a minimal difference of 10% in the photoelectrochemical performance, despite the tremendous variation in surface coverage.[44] In essence, the {001} and {101} facets afforded essentially identical performance, as we have shown herein. Thus, based on this previous result and our results, we do not expect significant variations in the photoelectrochemical performance as a result of minor facet impurity.

Our results demonstrate that sensitizing the {010} facet with the prototypical MK-2 organic dye leads to the best photoelectrochemical performance. In addition, our results also suggest that the {001} facet does not lead to improved performance relative to the {101} facet when sensitized with organic dyes. This contrasts with prior results using Ru-based dyes, which suggested that sensitizing the {001} facet led to marginal enhancements over the lowest energy {101} facet.[43−45]

3.4. Dye Loading and Dye Desorption Kinetics. A key element in rationalizing trends in the photoelectrochemical performance is characterization of the relative structures of the dye−semiconductor interfaces. For example, previous reports utilizing MK-2 and coumarin dyes have shown that the surface density of the dye and the degree of aggregation can significantly affect the performance.[34,51−53] The surface density of the MK-2 dye on the various TiO_2 faceted NPs are shown in Table 3. The results reveal that the {101}- and {010}-TiO_2 NPs have comparable surface densities of 0.84 and 0.87 molecules·nm^{-2}. However, the surface density for the {001}-TiO_2 is approximately half (0.51 molecules·nm^{-2}) of the value observed for the {101}. This result is interesting since the density of Ti^{4+} binding sites (Table 3) was calculated to be larger on the {001} facet relative to the {010} and {101} facets.

In prior reports, AFM measurements of TiO_2 single crystals sensitized with MK-2 show the formation of a monolayer of dye as well as accompanying aggregates of the dye.[38,52] In a recent study, dye desorption experiments further revealed that the MK-2 dye is adsorbed both as a covalently bound dye monolayer and as nonspecifically bound aggregates.[34,38,52] To investigate whether the variations in the surface coverage of MK-2 dye shown in Table 3 are a result of differences in the aggregation, we also determined the surface coverage of benzoic acid on the {001}, {101}, and {010} surfaces, since benzoic acid does not aggregate upon adsorption. Furthermore, the relatively simple structure of benzoic acid allows for more efficient computational modeling of the adsorbate/TiO_2 interface. As expected, benzoic acid has overall lower coverages than MK-2 on all of the surfaces, which is consistent with the fact that MK-2 is known to aggregate. More importantly, the surface coverage of benzoic acid displays a similar trend to the MK-2 dye with an approximate 2-fold decrease in the surface coverage in the {001} facet relative to the {101} and {010} facets.

Computational models of hydrated facets were constructed to investigate the lower surface coverage on the {001} facet relative to the {101} and {010} facets. A description of the computational methods and discussion of the structure of the water layer on the surface of the TiO_2 can be found in

DOI: 10.1021/ja5111078
J. Am. Chem. Soc. 2015, 137, 1520−1529

Sections 3 and 10 of the Supporting Information, respectively. Figure S8 depicts the calculated structures of the anhydrous and hydrated TiO_2 surfaces. In the case of the {101} and {010} facets, the Ti−O framework remained largely unchanged upon adsorption of water. On the other hand, hydration of the {001} facet with a monolayer of water molecules results in a significant structural reconfiguration of the TiO_2 surface. Specifically, the Ti−O−Ti bridges are broken by water molecules to form two hydroxide anions surrounding the Ti^{4+} surface sites. The remaining water molecules form bridging hydrogen-bond networks above every other row of Ti^{4+} sites on the reconstructed surface. The bridging hydrogen-bond networks are expected to sterically hinder the adsorption of carboxylate groups of either benzoic acid or MK-2 on the underlying Ti^{4+} sites, consistent with the lower surface coverage on the {001} facet relative to the {101} and {010} facets.[55]

Dye-desorption experiments were also performed to investigate the relative strength of the dye−surface interaction as a function of the different facets. The desorption curves as a function of time are shown in Figure 4. It is evident that the reaction reaches equilibrium after 1 h of desorption. At this point, the {010}-TiO_2 retains the largest amount of dye (∼11%) relative to the {101}-TiO_2 (∼4%) and the {001}-TiO_2 (<1%). Desorption curves were fit assuming a first-order model (cf. Section 9, Supporting Information) to determine the relevant kinetic parameters. The measured desorption rate constant (k_{des}, Table 3) of the {010}-TiO_2 was determined to be the lowest suggesting the best overall water stability. The increased water stability of the {010} facet has significant implications in terms of developing water-splitting photoelectrochemical devices since these devices operate in aqueous conditions. Interestingly, the dye is desorbed at the fastest rate from the {001} surface, and the rate constant was determined to be 36-fold higher than that of the {010} surface. The weaker covalent interaction between the MK-2 dye and {001} facet was further confirmed by calculating the adsorption energy of benzoic acid, used for facile computation, onto hydrated TiO_2 surfaces. Structures of the benzoic acid anchored with the commonly observed bridging bidentate and monodentate binding geometries are shown in Figure S9. The trends in calculated adsorption energy for both anchoring geometries suggest that the adsorption of benzoic acid is most energetically favorable in the case of {010}-TiO_2 and decreases significantly in the case of the {101}- and {001}-TiO_2, respectively, consistent with the dye-desorption experimental results.

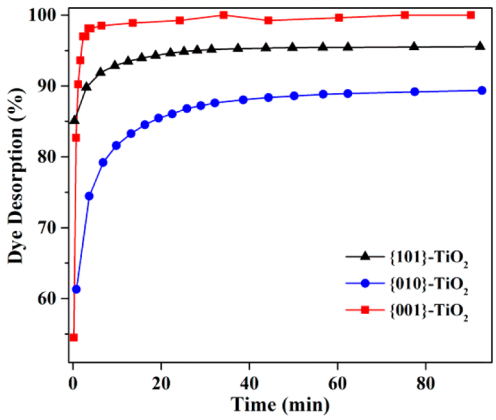

Figure 4. Time-dependent desorption curves for different faceted TiO_2/MK-2 samples.

3.5. Time-Resolved Spectroscopy. To investigate the mechanism of the facet-dependent photoelectrochemical performance, the electron injection and recombination dynamics (Figure 5) of MK-2 sensitized TiO_2 films were studied using time-resolved THz spectroscopy (TRTS) and TA spectroscopy. In TRTS, the photoexcitation of the surface-bound dye by a 400 nm pump beam leads to interfacial electron injection into the conduction band of TiO_2, and the formation of mobile charges affects the THz probe beam. The resulting THz transient can be utilized to determine the efficiency and rate of electron injection. The TRTS transients for the faceted NP films sensitized with MK-2 are shown in Figure 5A, and the first 25 ps after injection is highlighted in the inset. The injection efficiency for the different types of NPs can be quantitatively evaluated by observing the maximum attenuation of the THz probe beam (ΔTHz_{max}) after photoexcitation (cf. Section 11, Supporting Information), and the results are summarized in Table 4. The thickness of the films was sufficient such that all of the pump photons were absorbed, and thus, differences in the attenuation of the THz signal are attributed solely to relative differences in injection efficiency and not to differences in dye loading or SSA.[34] The results confirm that the {010}-TiO_2 has the highest injection efficiency, which is 1.3 and 1.7 times greater than the {101}- and {001}-TiO_2, respectively. The trend in electron injection efficiency is in excellent agreement with the EQE results, and these results

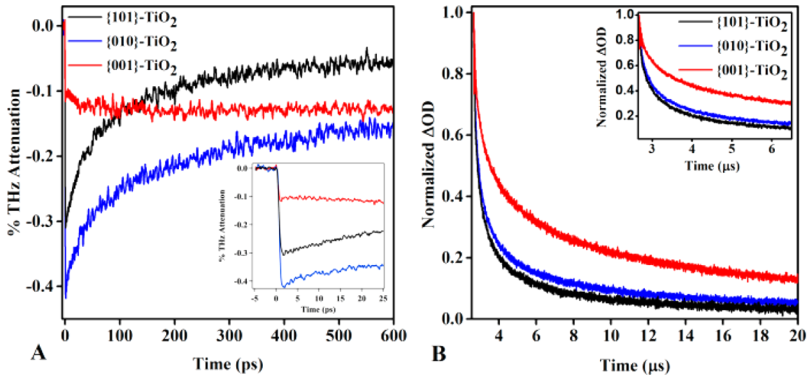

Figure 5. (A) Time-resolved THz transients collected from MK-2 sensitized faceted nanoparticle films after photoexcitation with a 400 nm pump beam. (B) Transient absorption curves measured at 800 nm for the decay of the charge-separated state of MK-2 sensitized faceted nanoparticle films after photoinduced electron injection from a pump beam at 560 nm. The insets show the first 25 ps and 7 μs of the TRTS and TA data, respectively.

DOI: 10.1021/ja5111078
J. Am. Chem. Soc. 2015, 137, 1520−1529

Table 4. Time-Resolved THz and TA Data

sample	ΔTHz_{max} (%)	τ_{ww} (μs)
{101}	0.30	0.96
{010}	0.40	1.39
{001}	0.13	5.44

collectively suggest that the {010}-TiO_2 is the most efficient at converting visible light to charge carriers.

In terms of electron-injection rate, the transients for the {010} and {101} films reveal that electron injection occurs within the 300 fs instrument response time. The subsequent recovery of the THz signal in the case of the {010}- and {101}-TiO_2 is attributed to trapping of mobile electrons.[31] On the other hand, the rate of injection in the {001}-TiO_2 is measurably slower as indicated by the onset of THz attenuation, which is slower than the instrument response time. Fitting an exponential function with an offset to the THz transient reveals that 80% of the THz attenuation occurs within the response time of the instrument (0−300 fs) and 20% occurs between 300 fs and 200 ps. The rate constant (k_{inj}) for electron injection beyond the instrument response time was determined to be 0.031 ps^{-1}. The slow rate of injection in the MK-2 sensitized {001}-TiO_2 film contrasts with the results from the {010}- and {101}-TiO_2 as well as prior results for MK-2 on commercial TiO_2 films (predominantly {101}-TiO_2),[34] which all find that 100% of electron injection occurs within the first 300 fs after photoexcitation. Since the driving force for injection is the same on all of the facets, the slow rate of injection suggests that the pathway for IET is not optimal in the case of the {001} surface.[29−31]

TA spectroscopy was performed to study the decay of the charge-separated state resulting from the recombination of conduction band electrons with the oxidized dye following electron injection. As shown in Figure 5B, the recombination rate of the MK-2 sensitized {010}- and {101}-TiO_2 films are comparable, while the {001}-TiO_2 film displays a much slower rate. The lifetimes (τ_{ww}) of the charge-separated state were determined from stretched exponential fits of the TA transients,[56] and the results are summarized in Table 4. The lifetime of the {001}-TiO_2 (5.44 μs) was 4 to 5 times longer than the lifetimes determined for {101}-TiO_2 (0.96 μs) and {010}-TiO_2 (1.36 μs).

The increased lifetime of the {001}-TiO_2 charge-separated state is consistent with our computational results discussed below and suggests that the pathway is longer and more difficult for IET in the case of the {001}-TiO_2. Although the rate of recombination is significantly lower for {001}-TiO_2, it is not enough to offset the weak covalent interaction and poor injection efficiency which leads to the low J_{sc} and EQE relative to the {010} and {101} facets.

3.6. IET Simulations. Simulations were carried out using the IET code developed previously by Batista and co-workers[36,57−59] (cf. Section 3 of Supporting Information), and the results are summarized in Figure 6. In this case, the survival probability (SP) represents the probability for the electron to remain either on the photoexcited dye as shown in Figure 6A or on the photoexcited dye and TiO_2 cluster as shown in Figure 6B. In essence, the SP shown in Figure 6A simulates the injection of the electron into the TiO_2 cluster, and the corresponding SP shown in Figure 6B simulates the formation of the charge-separated state as the electron density passes from the TiO_2 cluster into the absorbing potential at the bottom of the slab. We selected a distance of ~7.7 Å between the top layer and the bottom layer where the adsorbing potential is applied for each slab so that the simulation of the charge-separation effect is consistent among the different facets. Figure 6A, B are overlaid in Figure S11 allowing for ease of comparison.

The injection efficiencies calculated for each surface at 1000 fs are summarized in Table 5 and are in excellent agreement with the experimental trend observed by TRTS. Specifically, the rate of electron injection in the case of the {001} facet is considerably slower than the rate measured for the {101} and {010} facets. It is evident from Figure 6B that the formation of the charge-separated state in the case of the {010} and {001} surfaces has a rapid component between 0 and 200 fs, wherein about 50% of the injection occurs. On the other hand, the injection into the {001} surface is nearly linear and has a much slower overall rate between 0 and 200 fs, wherein only about 10% of injection occurs.

Table 5. Summary of Injection Simulation Results for the Different TiO_2 Facets Including Injection Efficiency, Length of the Injection Pathway, and the Number of Atoms along Injection Pathway

sample	injection at 1000 fs (%)	slab thickness (Å)	length of injection pathway (Å)	no. of atoms along injection pathway
{101}	55	7.7	7.9	4
{010}	75	7.7	7.9	4
{001}	35	7.7	11.9	6

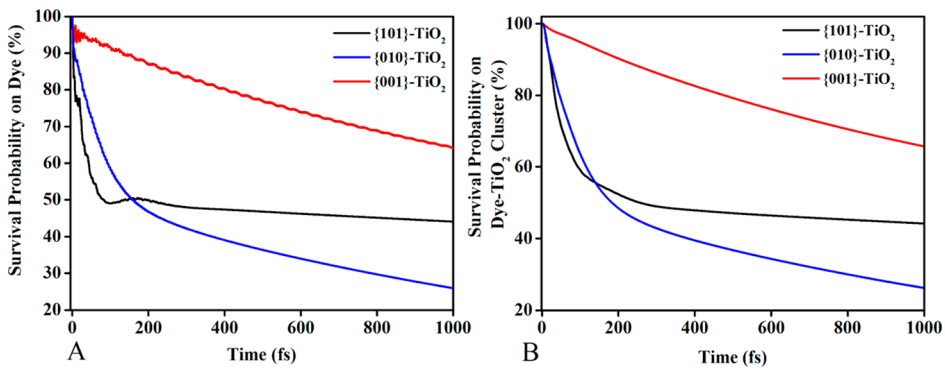

Figure 6. Simulation results for the injection from MK-2 dye bound to the {101}, {010}, and {001} facets via a bridging bidentate interaction. The results are shown as survival probability of electron density on the (A) MK-2 dye and the (B) MK-2 dye and TiO_2 cluster as a function of time.

DOI: 10.1021/ja5111078
J. Am. Chem. Soc. 2015, 137, 1520−1529

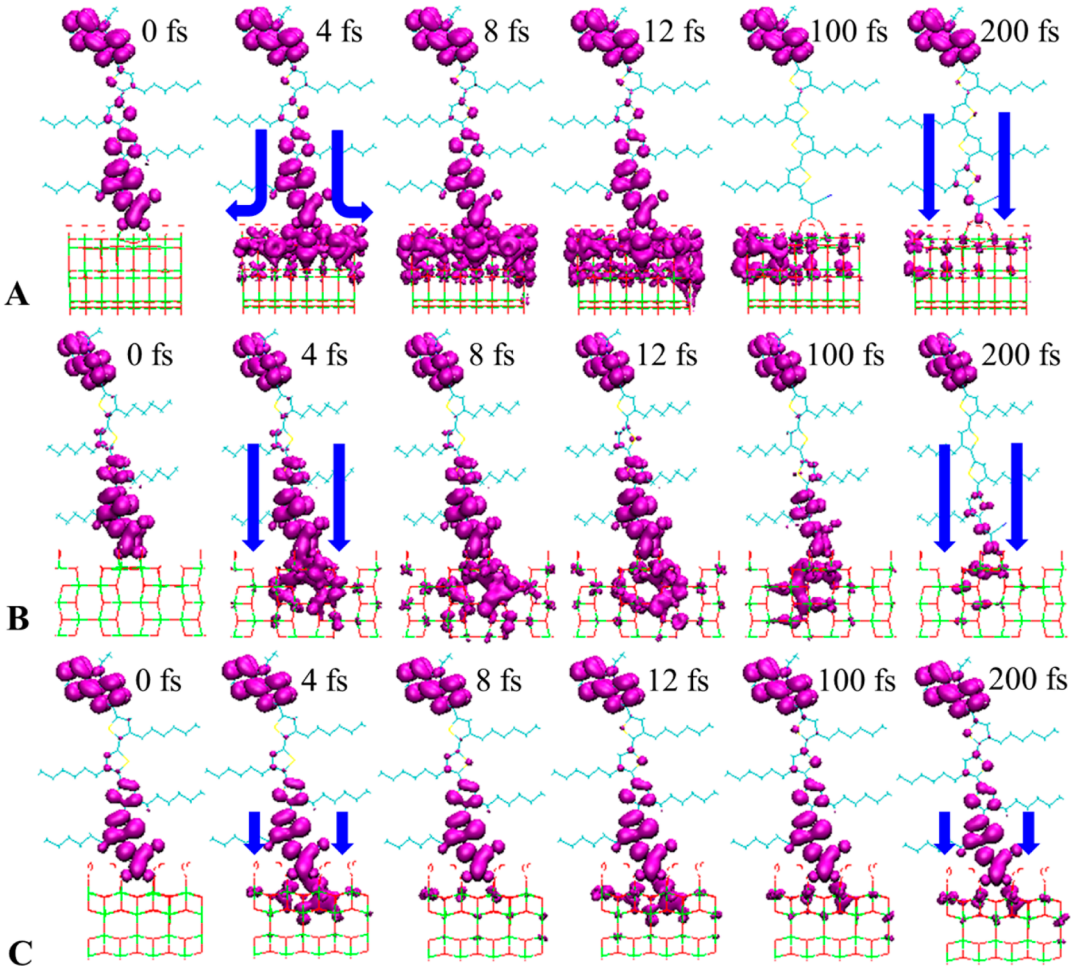

Figure 7. Snapshots of electron density calculated at 0, 4, 8, 12, 100, and 200 fs for the (A) {101}, (B) {010}, and (C) {001} facets. The blue arrows denote the direction electron density as it is injected into the TiO_2 facets at the different times.

To investigate the differences in the relative rates of injection, representative snapshots of the electron density distribution for each surface between 0 and 200 fs are shown in Figure 7 (the injection simulation is shown in Supporting Information). The snapshots at 8 and 12 fs for the {010} surface reveal that the pathway of electron injection is direct, leading to very efficient transfer of the wavepacket through the TiO_2 cluster. This is consistent with the SP trends in Figure 6, which indicates that injection into the cluster and formation of the charge-separated state occur almost simultaneously. On the other hand, injection into the {101} facet is initially very rapid between 0−8 fs but leads to a concentration of the electron density in the first two layers of the cluster between 8−100 fs. The injection then proceeds downward toward the bottom of the cluster between 12 and 200 fs. This concentration of the electron density on the first and second layers of the cluster is apparent in Figure 6 by the delay between the injection of electrons into the cluster and the formation of the charge-separated state. This effect may contribute to the lower overall injection efficiency of the {101} surface relative to the {010} surface, since concentration of the electron density at the surface for the first 8−100 fs may lead to higher probability of recombination of the injected wavepacket with the excited state of the MK-2 dye during injection.

The slow rate of electron injection and the low injection efficiency of the {001} surface relative to the {010} and {101} surfaces can be rationalized by the structure of the different facets, and the snapshots of the electron density distribution show that it is qualitatively different. In the case of the {001} surface, the wavepacket remains largely localized on the dye molecule even after 200 fs, whereas most of the electron density has already been injected into the slab at this point in the case of the {010} and {101} surfaces. Examination of the structures of the different surfaces reveals that the pathway for charge separation requires only four vertical hops for the {010} and {101} surfaces. The distance required for these hops is approximately 7.9 Å, which is comparable to the overall thickness of the slab. On the other hand, the structure of the {001} facet requires that the electron travel over a total of six atoms that includes three horizontal hops and three vertical hops. This leads to a path length of 11.9 Å in order for the wavepacket to traverse the 7.7 Å thickness of the slab and encounter the absorbing boundary. In addition, our results indicate that there is a significant barrier for electron movement between the second and third layer of atoms on the {001} facet since most of the injected electron density resides in the first two layers atoms even after 200 fs. This result suggests that the horizontal hop required to traverse from the second to the third layer slows propagation of the wavepacket to the third layer of atoms and, therefore, slows overall electron injection into this surface.

These computational results provide unique insights into the TRTS and TA results. Based on our results, the trend in

DOI: 10.1021/ja5111078
J. Am. Chem. Soc. 2015, 137, 1520−1529

injection efficiency determined by TRTS can be related to the pathway of electron injection in the different surfaces. We find that the {010} surface has the most efficient and direct pathway compared to the {101} and {001} surfaces, thereby explaining the highest overall injection efficiency. In terms of the TA results, the {001} facet was found to have the longest lifetime of the charge-separated state. This is not surprising since these computational results reveal that the electron-transfer pathway is considerably longer and has a barrier in the case of {001} facet. Thus, it is not surprising that recombination of injected electrons with the dye cation is slower in the {001} surface since the pathway for recombination is more difficult.

4. CONCLUSION

This article has presented a systematic study of the facet-dependent photoelectrochemical performance of TiO_2 nanomaterials with predominantly exposed {101}-, {010}-, and {001}-TiO_2 surfaces. The methyl orange photodegradation performance was mainly dependent on surface energy and density of under-coordinated Ti^{4+} sites. Facet-dependent photoelectrochemical activity was quantified using MK-2 sensitized solar cells. Solar cell characterizations indicated that {010}-TiO_2-based cells evince the highest overall efficiency (6.1%) compared with devices prepared with {001}- and {101}-TiO_2. The trend in facet-dependent performance was extensively probed by time-resolved spectroscopic studies such as picosecond THz and nanosecond TA spectroscopies to measure the electron injection and recombination dynamics. The results demonstrate that the increased performance is due to a favorable increase in the injection efficiency of the MK-2 dye on the {010} facet relative to the {101} and {001} facets. Computational results demonstrate that this is because {010} facet provides the most rapid and direct pathway for IET, thereby leading to the highest conversion of visible light to charge carriers.

■ ASSOCIATED CONTENT

Ⓢ Supporting Information

Additional details regarding the synthesis and characterization of the faceted TiO_2 nanoparticles, time-resolved spectroscopic techniques, and computational methods. Also included are additional details regarding the photodegradation reactions, absorption spectrum of the MK-2 dye, computational models of the hydrated TiO_2 surfaces, and analysis of the desorption kinetics and TRTS results. This material is available free of charge via the Internet at http://pubs.acs.org.

■ AUTHOR INFORMATION

Corresponding Authors

*jaehong.kim@yale.edu

*charles.schmuttenmaer@yale.edu

Author Contributions

[§]These authors contributed equally.

Notes

The authors declare no competing financial interest.

■ ACKNOWLEDGMENTS

This work was funded by the U.S. Department of Energy Office of Science, Office of Basic Energy Sciences, under award no. DE-FG02-07ER15909 (V.S.B, G.W.B., and C.A.S.), by a generous donation from the TomKat Charitable Trust and by the National Science Foundation under grant no. 1235916 (J.H.K.). The computational work was supported by the facilities and staff of the Yale University Faculty of Arts and Sciences High Performance Computing Center and by the National Science Foundation under grant no. CNS08-21132 that partially funded acquisition of these facilities. We also thank Dr. Christian F. A. Negre for providing his code to construct the water-free pristine TiO_2 surfaces for all three facets and for relevant discussion regarding the computation results.

■ REFERENCES

(1) Li, C.; Wang, F.; Yu, J. C. *Energy Environ. Sci.* **2011**, *4*, 100.

(2) Hagfeldt, A.; Boschloo, G.; Sun, L.; Kloo, L.; Pettersson, H. *Chem. Rev.* **2010**, *110*, 6595.

(3) Neo, D. C. J.; Cheng, C.; Stranks, S. D.; Fairclough, S. M.; Kim, J. S.; Kirkland, A. I.; Smith, J. M.; Snaith, H. J.; Assender, H. E.; Watt, A. A. R. *Chem. Mater.* **2014**, *26*, 4004.

(4) Wang, Q.; Hisatomi, T.; Ma, S. S. K.; Li, Y.; Domen, K. *Chem. Mater.* **2014**, *26*, 4144.

(5) Chen, C.; Ma, W.; Zhao, J. *Chem. Soc. Rev.* **2010**, *39*, 4206.

(6) Chen, X.; Mao, S. S. *Chem. Rev.* **2007**, *107*, 2891.

(7) Hu, X.; Li, G.; Yu, J. C. *Langmuir* **2009**, *26*, 3031.

(8) Bai, Y.; Mora-Seró, I.; De Angelis, F.; Bisquert, J.; Wang, P. *Chem. Rev.* **2014**, *114*, 10095.

(9) Pagliaro, M.; Palmisano, G.; Ciriminna, R.; Loddo, V. *Energy Environ. Sci.* **2009**, *2*, 838.

(10) Fujishima, A.; Zhang, X.; Tryk, D. A. *Surf. Sci. Rep.* **2008**, *63*, 515.

(11) Liu, G.; Yu, J. C.; Lu, G. Q.; Cheng, H.-M. *Chem. Commun.* **2011**, *47*, 6763.

(12) Howard, C. J.; Sabine, T. M.; Dickson, F. *Acta Crystallogr., Sect. B: Struct. Sci.* **1991**, *47*, 462.

(13) Yang, H. G.; Liu, G.; Qiao, S. Z.; Sun, C. H.; Jin, Y. G.; Smith, S. C.; Zou, J.; Cheng, H. M.; Lu, G. Q. *J. Am. Chem. Soc.* **2009**, *131*, 4078.

(14) Yang, H. G.; Sun, C. H.; Qiao, S. Z.; Zou, J.; Liu, G.; Smith, S. C.; Cheng, H. M.; Lu, G. Q. *Nature* **2008**, *453*, 638.

(15) Zhang, D.; Li, G.; Wang, H.; Chan, K. M.; Yu, J. C. *Cryst. Growth Des.* **2010**, *10*, 1130.

(16) Pan, J.; Liu, G.; Lu, G. Q.; Cheng, H.-M. *Angew. Chem., Int. Ed.* **2011**, *50*, 2133.

(17) Amano, F.; Yasumoto, T.; Prieto-Mahaney, O.-O.; Uchida, S.; Shibayama, T.; Ohtani, B. *Chem. Commun.* **2009**, 2311.

(18) Hosono, E.; Fujihara, S.; Imai, H.; Honma, I.; Masaki, I.; Zhou, H. *ACS Nano* **2007**, *1*, 273.

(19) Mao, Y.; Wong, S. S. *J. Am. Chem. Soc.* **2006**, *128*, 8217.

(20) Barnard, A. S.; Curtiss, L. A. *Nano Lett.* **2005**, *5*, 1261.

(21) Ong, W.-J.; Tan, L.-L.; Chai, S.-P.; Yong, S.-T.; Mohamed, A. R. *Nanoscale* **2014**, *6*, 1946.

(22) Liu, S.; Yu, J.; Jaroniec, M. *Chem. Mater.* **2011**, *23*, 4085.

(23) Zhang, D.; Li, G.; Yang, X.; Yu, J. C. *Chem. Commun.* **2009**, 4381.

(24) Duan, L.; Tong, L.; Xu, Y.; Sun, L. *Energy Environ. Sci.* **2011**, *4*, 3296.

(25) Swierk, J. R.; Mallouk, T. E. *Chem. Soc. Rev.* **2013**, *42*, 2357.

(26) Jung, H. S.; Lee, J.-K. *J. Phys. Chem. Lett.* **2013**, *4*, 1682.

(27) Halme, J.; Vahermaa, P.; Miettunen, K.; Lund, P. *Adv. Mater.* **2010**, *22*, E210.

(28) Young, K. J.; Martini, L. A.; Milot, R. L.; Snoeberger Iii, R. C.; Batista, V. S.; Schmuttenmaer, C. A.; Crabtree, R. H.; Brudvig, G. W. *Coord. Chem. Rev.* **2012**, *256*, 2503.

(29) Koops, S. E.; O'Regan, B. C.; Barnes, P. R. F.; Durrant, J. R. *J. Am. Chem. Soc.* **2009**, *131*, 4808.

(30) Koops, S. E.; Barnes, P. R. F.; O'Regan, B. C.; Durrant, J. R. *J. Phys. Chem. C* **2010**, *114*, 8054.

(31) Milot, R. L.; Moore, G. F.; Crabtree, R. H.; Brudvig, G. W.; Schmuttenmaer, C. A. *J. Phys. Chem. C* **2013**, *117*, 21662.

DOI: 10.1021/ja5111078
J. Am. Chem. Soc. 2015, 137, 1520−1529

(32) McNamara, W. R.; Milot, R. L.; Song, H.-E.; Snoeberger, R. C.; Batista, V. S.; Schmuttenmaer, C. A.; Brudvig, G. W.; Crabtree, R. H. *Energy Environ. Sci.* **2010**, *3*, 917.
(33) McNamara, W. R.; Snoeberger, R. C.; Li, G.; Richter, C.; Allen, L. J.; Milot, R. L.; Schmuttenmaer, C. A.; Crabtree, R. H.; Brudvig, G. W.; Batista, V. S. *Energy Environ. Sci.* **2009**, *2*, 1173.
(34) Koenigsmann, C.; Ripolles, T. S.; Brennan, B. J.; Negre, C. F. A.; Koepf, M.; Durrell, A. C.; Milot, R. L.; Torre, J. A.; Crabtree, R. H.; Batista, V. S.; Brudvig, G. W.; Bisquert, J.; Schmuttenmaer, C. A. *Phys. Chem. Chem. Phys.* **2014**, *16*, 16629.
(35) Brennan, B. J.; Llansola Portoles, M. J.; Liddell, P. A.; Moore, T. A.; Moore, A. L.; Gust, D. *Phys. Chem. Chem. Phys.* **2013**, *15*, 16605.
(36) Rego, L. G. C.; Batista, V. S. *J. Am. Chem. Soc.* **2003**, *125*, 7989.
(37) Negre, C. F. A.; Fuertes, V. C.; Oviedo, M. B.; Oliva, F. Y.; Sánchez, C. G. *J. Phys. Chem. C* **2012**, *116*, 14748.
(38) Nepomnyashchii, A. B.; Parkinson, B. A. *Langmuir* **2013**, *29*, 9362.
(39) Santulli, A. C.; Koenigsmann, C.; Tiano, A. L.; DeRosa, D.; Wong, S. S. *Nanotechnology* **2011**, *22*, 245402.
(40) Park, T.-J.; Levchenko, A. A.; Zhou, H.; Wong, S. S.; Navrotsky, A. *J. Mater. Chem.* **2010**, *20*, 8639.
(41) Etgar, L.; Zhang, W.; Gabriel, S.; Hickey, S. G.; Nazeeruddin, M. K.; Eychmüller, A.; Liu, B.; Grätzel, M. *Adv. Mater.* **2012**, *24*, 2202.
(42) De Angelis, F.; Vitillaro, G.; Kavan, L.; Nazeeruddin, M. K.; Grätzel, M. *J. Phys. Chem. C* **2012**, *116*, 18124.
(43) Yu, J.; Fan, J.; Lv, K. *Nanoscale* **2010**, *2*, 2144.
(44) Wu, X.; Chen, Z.; Qing, G.; Lu, G. Q.; Wang, L. *Adv. Funct. Mater.* **2011**, *21*, 4167.
(45) Yang, W.; Li, J.; Wang, Y.; Zhu, F.; Shi, W.; Wan, F.; Xu, D. *Chem. Commun.* **2011**, *47*, 1809.
(46) Ito, S.; Chen, P.; Comte, P.; Nazeeruddin, M. K.; Liska, P.; Péchy, P.; Grätzel, M. *Prog. Photovoltaics* **2007**, *15*, 603.
(47) Dürr, M.; Rosselli, S.; Yasuda, A.; Nelles, G. *J. Phys. Chem. B* **2006**, *110*, 21899.
(48) Roy, N.; Sohn, Y.; Pradhan, D. *ACS Nano* **2013**, *7*, 2532.
(49) Yu, J.; Low, J.; Xiao, W.; Zhou, P.; Jaroniec, M. *J. Am. Chem. Soc.* **2014**, *136*, 8839.
(50) Kim, B.-G.; Chung, K.; Kim, J. *Chem.—Eur. J.* **2013**, *19*, 5220.
(51) Wang, Z.-S.; Cui, Y.; Dan-oh, Y.; Kasada, C.; Shinpo, A.; Hara, K. *J. Phys. Chem. C* **2008**, *112*, 17011.
(52) Wang, Z.-S.; Koumura, N.; Cui, Y.; Takahashi, M.; Sekiguchi, H.; Mori, A.; Kubo, T.; Furube, A.; Hara, K. *Chem. Mater.* **2008**, *20*, 3993.
(53) Sewvandi, G. A.; Chen, C.; Ishii, T.; Kusunose, T.; Tanaka, Y.; Nakanishi, S.; Feng, Q. *J. Phys. Chem. C* **2014**, *118*, 20184.
(54) Finnie, K. S.; Bartlett, J. R.; Woolfrey, J. L. *Langmuir* **1998**, *14*, 2744.
(55) Vittadini, A.; Selloni, A.; Rotzinger, F. P.; Grätzel, M. *Phys. Rev. Lett.* **1998**, *81*, 2954.
(56) Abrahamsson, M.; Johansson, P. G.; Ardo, S.; Kopecky, A.; Galoppini, E.; Meyer, G. J. *J. Phys. Chem. Lett.* **2010**, *1*, 1725.
(57) Abuabara, S. G.; Rego, L. G. C.; Batista, V. S. *J. Am. Chem. Soc.* **2005**, *127*, 18234.
(58) Snoeberger Iii, R. C.; Lian, T.; Batista, V. S. In *Proceedings of SPIE 7396, Physical Chemistry of Interfaces and Nanomaterials VIII*; Monti, O. L. A., Prezhdo, O. V., Eds.; SPIE: Bellingham, WA, 2009; Vol. *7396*, p 739604.
(59) Snoeberger, R. C.; Young, K. J.; Tang, J.; Allen, L. J.; Crabtree, R. H.; Brudvig, G. W.; Coppens, P.; Batista, V. S.; Benedict, J. B. *J. Am. Chem. Soc.* **2012**, *134*, 8911.

DOI: 10.1021/ja5111078
J. Am. Chem. Soc. 2015, 137, 1520−1529